International Journal of Solids and Structures 147 (2018) 156–165

Contents lists available at ScienceDirect

International Journal of Solids and Structures

journal homepage: www.elsevier.com/locate/ijsolstr

Viscoplasticity of voided cubic crystals under hydrostatic loading

Louis Joëssel[a], Pierre-Guy Vincent[a,c], Mihail Gărăjeu[b], Martín I. Idiart[d,e,*]

[a] Institut de Radioprotection et de Sûreté Nucléaire (IRSN), BP 3, Saint-Paul-Lez-Durance cedex 13115, France
[b] Aix Marseille Université, CNRS, Centrale Marseille, LMA, Marseille F-13453, France
[c] Laboratoire de Micromécanique et d'Intégrité des Structures (MIST), IRSN-CNRS-UM, BP 3, Saint-Paul-Lez-Durance cedex 13115, France
[d] Departamento de Aeronáutica, Facultad de Ingeniería, Universidad Nacional de La Plata, Avda. 1 esq. 47, La Plata B1900TAG, Argentina
[e] Consejo Nacional de Investigaciones Científicas y Técnicas (CONICET), CCT La Plata, Calle 8 N 1467, La Plata B1904CMC, Argentina

ARTICLE INFO

Article history:
Received 27 October 2017
Revised 12 May 2018
Available online 6 June 2018

Keywords:
Crystalline solids
Porosity
Viscoplasticity
Micromechanics
Homogenization

ABSTRACT

A micromechanical study of the viscoplasticity of voided cubic crystals is presented. The microscopic void distribution is isotropic and the macroscopic loading is hydrostatic. Three different approaches are considered. The first approach consists in idealizing the voided crystal as a hollow sphere assemblage and bounding from above the corresponding dissipation potential *à la* Gurson. The second approach consists in idealizing the voided crystal as a sequential laminate of infinite rank and computing the corresponding dissipation potential exactly. Finally, the third approach consists in idealizing the voided crystal as a periodic medium with a complex unit cell and computing the mechanical fields numerically via a Fast Fourier Transform (FFT) algorithm. Predictions are reported for a wide range of crystals deforming by power-law creep and rate-independent plasticity. When the plastic anisotropy is weak, a fairly good agreement between all three approaches is observed. When the plastic anisotropy is strong, by contrast, discrepancies arise. In the extreme case of plastically deficient crystals, the various predictions can exhibit different asymptotics. While estimates based on hollow-sphere assemblages predict that any deficient voided crystal is rigid under hydrostatic loading, FFT simulations and sequential laminates suggest that some deficient voided crystals with more than two linearly independent systems may dilate. Overall, estimates based on sequential laminates are found to be superior to Gurson-type estimates based on hollow sphere assemblages and to predict the hydrostatic response of cubic voided crystals with reasonable accuracy, even for relatively strong plastic anisotropies.

1. Introduction

Some engineering alloys employed in nuclear reactors can nucleate intragranular voids when exposed to prolonged neutronic irradiation (e.g., Garner, 2012). In the concomitant presence of high temperatures and mechanical stresses, the voids may subsequently grow by creep deformation to the extent of compromising the mechanical integrity of the material. Experimental and numerical studies on the viscoplasticity of single crystals have shown that crystal anisotropy can have a significant impact on the void growth process (e.g., Crépin et al., 1996; Yerra et al., 2010; Srivastava and Needleman, 2013). This has motivated recent efforts to incorporate crystal anisotropy into constitutive models for viscoplastic voided solids. One of the first proposals was made by Han et al. (2013). These authors confected a yield function for voided cubic crystals by combining elements from the linear-comparison homogenization approach of de Botton and Ponte Castañeda (1995) for crystalline solids and the limit analysis of Gurson (1977) for isotropic solids. The model was further improved by introducing Tvergaard-type parameters that were adjusted with finite-element calculations for periodic solids. One of these parameters impacts the predictions for high stress triaxialities by directly rescaling the hydrostatic mean stress. An alternative yield function was subsequently proposed by Paux et al. (2015). These authors regularized the Bishop–Hill polyhedron of the crystalline matrix and exploited the limit analysis of Benzerga and Besson (2001) for Hill-type solids. As in the previous case, however, the hydrostatic mean stress was rescaled to improve predictions for high stress triaxialities. A more comprehensive constitutive model, allowing for any crystal symmetry and incorporating power-law viscoplasticity as well as void shape effects, was proposed by Mbiakop et al. (2015). The model is based on the linear-comparison approach of de Botton and Ponte Castañeda (1995) with an ad-hoc class of comparison creep compliances suitably chosen so that, once again, predictions for purely

* Corresponding author at: Departamento de Aeronáutica, Facultad de Ingeniería, Universidad Nacional de La Plata, Avda. 1 esq. 47, La Plata B1900TAG, Argentina.
E-mail addresses: joessel@lma.cnrs-mrs.fr (L. Joëssel), pierre-guy.vincent@irsn.fr (P.-G. Vincent), mihai.garajeu@univ-amu.fr (M. Gărăjeu), martin.idiart@ing.unlp.edu.ar (M.I. Idiart).

https://doi.org/10.1016/j.ijsolstr.2018.05.022
0020-7683/

hydrostatic loadings reduce to certain reference values. More recently, Song and Castañeda (2017) made use of a more sophisticated linear-comparison approach to derive a fairly general constitutive model incorporating deformation-induced microstructural changes. This approach includes an iterative procedure that serves to improve the predictions at high stress triaxialities. It is thus evident that hydrostatic loadings are of particular relevance to the development of constitutive models of this sort. Motivated by this observation, we report a detailed analysis of a viscoplastic single crystal containing an isotropic distribution of voids and deforming under remote hydrostatic stresses, which could serve as a reference for adjusting more general constitutive models. Additional interest on this analysis stems from the fact that hydrostatic loadings usually exacerbate differences between competing theories and, furthermore, allow analytical treatment. Three different approaches are considered.

The first approach consists in idealizing the voided crystal as a hollow sphere assemblage and then bounding from above the associated dissipation potential by evaluating the relevant functional at spherical velocity fields. This approach was initially proposed by Gurson (1977) to model void growth in isotropic plastic solids, and has been extensively employed since then in more general contexts by numerous investigators in view of its accuracy and simplicity (see Benzerga and Leblond, 2010 and references therein). The vast majority of such works have retained the assumption of local isotropy presumably because the resulting bounds turn out to be exact only when this condition holds. Strictly, however, Gurson's approach does apply to locally anisotropic solids as well (Benzerga and Besson, 2001; Paux et al., 2015), even though its accuracy is expected to deteriorate with increasing plastic anisotropy. Assessing this expectation is one of the objectives of the present work.

The second approach consists in idealizing the voided crystal as a sequential laminate of infinite rank obeying an isotropic lamination sequence initially proposed by de Botton (2005) in a two-dimensional context and later generalized by Idiart (2008), and computing the associated dissipation potential exactly. While geometrically unrealistic at first sight, these sequentially laminated microstructures have been found to realistically mimic a wide variety of two-phase material systems including viscoplastic voided solids (e.g., Idiart, 2008; Danas et al., 2008). Interestingly, these sequential laminates exhibit the exact same response as a hollow sphere assemblage under hydrostatic loading when the porosity distribution and local response are both isotropic (Idiart, 2007; 2008). In contrast to Gurson's approach, however, this approach yields an exact result for sequentially laminated systems even when the matrix is locally anisotropic; it is therefore expected to be more accurate, especially for highly anisotropic crystals. Assessing this expectation is another objective of the present work.

Finally, the third approach consists in idealizing the voided crystal as a periodic medium with a complex unit cell, and computing the mechanical fields numerically via a Fast Fourier Transform (FFT) algorithm proposed by Moulinec and Suquet (1994). The FFT method makes direct use of microstructural images and is particularly suitable for investigating strongly nonlinear material responses that can lead to severe localization of the mechanical fields (e.g., Idiart et al., 2006; Idiart et al., 2009, and Grennerat et al., 2012), as expected in the present work. These numerical results are adopted as benchmarks to assess the accuracy of the other two approaches.

2. Problem formulation

2.1. Local properties

We consider a representative volume element (RVE) of the voided crystal containing a statistically uniform distribution of voids whose characteristic size is much smaller than that of the RVE. The crystalline matrix is identified as phase $r = 1$ while the voids are collectively identified as phase $r = 2$. Viscoplasticity is most conveniently studied by adopting an Eulerian description of motion. Thus, we consider a generic stage of deformation where the domains occupied by the crystalline matrix, the voids, and the RVE are $\Omega^{(1)}$, $\Omega^{(2)}$ and $\Omega = \Omega^{(1)} \cup \Omega^{(2)}$, respectively. The distribution of voids is taken to be isotropic.

The crystalline matrix is assumed to deform by multi-glide along K slip systems following a purely viscoplastic response characterized by a convex dissipation potential w such that the Cauchy stress $\boldsymbol{\sigma}$ and Eulerian strain rate $\boldsymbol{D}$ tensors are related by

$$\boldsymbol{\sigma} = \partial_{\boldsymbol{D}} w(\boldsymbol{D}). \tag{1}$$

In the case of power-law standard viscoplasticity, the dissipation potential is given by

$$w(\boldsymbol{D}) = \sup_{\boldsymbol{\sigma}} [\boldsymbol{\sigma}\cdot\boldsymbol{D} - u(\boldsymbol{\sigma})] \quad \text{with} \quad u(\boldsymbol{\sigma}) = \sum_{k=1}^{K} \frac{\tau_0^{(k)}\dot{\gamma}_0}{n+1} \left| \frac{\boldsymbol{\sigma}\cdot\boldsymbol{\mu}^{(k)}}{\tau_0^{(k)}} \right|^{n+1}, \tag{2}$$

where the stress potential u is the Legendre dual of w. In this last expression, $n \geq 1$ is the creep exponent, $\dot{\gamma}_0$ is a reference strain rate, and $\tau_0^{(k)} > 0$ is the flow stress of the kth slip system with Schmid tensor $\boldsymbol{\mu}^{(k)} = \mathbf{n}^{(k)} \otimes_s \mathbf{m}^{(k)}$, normal vector $\mathbf{n}^{(k)}$, and flow direction $\mathbf{m}^{(k)}$. Henceforth, $\otimes$, $\otimes_s$ and $\otimes_d$ will denote the tensor product, its symmetric part, and its deviatoric part, respectively. In this work we restrict attention to families of slip systems such that the crystal response exhibits cubic symmetry. Note that the Schmid tensors are traceless and therefore the potential (2) characterizes an incompressible response. Furthermore, note that the stress potential u is homogeneous of degree $n+1$ and 1 in $\boldsymbol{\sigma}$ and $\dot{\gamma}_0$, respectively, and therefore the dissipation potential w is homogeneous of degree $1+1/n$ and $-1/n$ in $\boldsymbol{D}$ and $\dot{\gamma}_0$.

Power-law viscoplasticity is particularly appropriate for investigating the effect of nonlinearity and crystal anisotropy in a wide range of material behaviors. The limiting cases $n = 1$ and $n \to \infty$ correspond to linearly viscous and rate-independent plastic behaviors, respectively. In the former case, the dissipation potential becomes

$$w(\boldsymbol{D}) = \begin{cases} \frac{1}{2}\boldsymbol{D}_d \cdot \mathbb{L}\boldsymbol{D}_d & \text{if } \mathrm{tr}\boldsymbol{D} = 0, \\ +\infty & \text{otherwise}, \end{cases} \tag{3}$$

where $\boldsymbol{D}_d$ is the deviatoric part of $\boldsymbol{D}$ and $\mathbb{L} = [\sum_{k=1}^{K} (\tau_0^{(k)}/\dot{\gamma}_0)^{-1} \boldsymbol{\mu}^{(k)} \otimes \boldsymbol{\mu}^{(k)}]^{-1}$ is an incompressible viscosity tensor. In the latter case, the dissipation potential becomes

$$w(\boldsymbol{D}) = \begin{cases} \sup\limits_{\boldsymbol{\sigma}_d \in \mathcal{P}} \boldsymbol{\sigma}_d \cdot \boldsymbol{D}_d & \text{if } \mathrm{tr}\boldsymbol{D} = 0, \\ +\infty & \text{otherwise}, \end{cases} \tag{4}$$

where the set $\mathcal{P} = \left\{ \boldsymbol{\sigma}_d \in \mathcal{T}_d \ : \ |\boldsymbol{\sigma}_d \cdot \boldsymbol{\mu}^{(k)}| \leq \tau_0^{(k)}, \ k = 1, \ldots, K \right\}$ represents the strength domain of the crystalline matrix, and $\mathcal{T}_d$ is the set of deviatoric symmetric second-order tensors. Since the boundary of this strength domain is a polyhedron in the space of deviatoric stresses, the supremum in (4) must be attained at a vertex of the polyhedron. Thus, we can also write

$$w(\boldsymbol{D}) = \begin{cases} \max\limits_{\boldsymbol{\sigma}_d \in \mathcal{V}} \boldsymbol{\sigma}_d \cdot \boldsymbol{D}_d & \text{if } \mathrm{tr}\boldsymbol{D} = 0, \\ +\infty & \text{otherwise}, \end{cases} \tag{5}$$

where $\mathcal{V}$ denotes the set of vertices of the strength domain.

2.2. Effective properties

The macroscopic response of the voided crystal is defined as the relation between the volume averages of the Cauchy stress and

Eulerian strain-rate fields over the RVE. Formally, it can be characterized by an effective dissipation potential $\tilde{w}$ such that (e.g., Castañeda and Suquet, 1998)

$$\bar{\boldsymbol{\sigma}} = \partial_{\bar{\boldsymbol{D}}}\tilde{w}(\bar{\boldsymbol{D}}), \quad \tilde{w}(\bar{\boldsymbol{D}}) = (1-f)\min_{\boldsymbol{D}(\boldsymbol{x})\in\mathcal{K}(\bar{\boldsymbol{D}})}\frac{1}{|\Omega^{(1)}|}\int_{\Omega^{(1)}} w(\boldsymbol{D}(\boldsymbol{x}))\,\mathrm{d}\Omega, \tag{6}$$

where $f = |\Omega^{(2)}|/|\Omega|$ is the volume fraction occupied by the voids, i.e. the porosity, and $\mathcal{K}(\bar{\boldsymbol{D}})$ is the set of kinematically admissible strain-rate fields $\mathcal{K}(\bar{\boldsymbol{D}}) = \left\{\boldsymbol{D}:\Omega\to\mathcal{T} \;:\; \boldsymbol{D}(\boldsymbol{x}) = \nabla\otimes_s \boldsymbol{u}(\boldsymbol{x}) \text{ in } \Omega \wedge \boldsymbol{u} = \bar{\boldsymbol{D}}\boldsymbol{x} \text{ on } \partial\Omega\right\}$.

In view of the assumed isotropy of the void distribution, the effective potential $\tilde{w}$ inherits the cubic symmetry from the local potential w. A hydrostatic stress $\bar{\boldsymbol{\sigma}} = \bar{\sigma}_m\boldsymbol{I}$ thus produces a spherical strain rate $\bar{\boldsymbol{D}} = \bar{D}_m\boldsymbol{I}$. In this case, the effective constitutive relation (6) reduces to

$$\bar{\sigma}_m = \frac{1}{3}\partial_{\bar{D}_m}\tilde{w}_h(\bar{D}_m) \quad \text{where} \quad \tilde{w}_h(\bar{D}_m) = \tilde{w}(\bar{D}_m\boldsymbol{I}). \tag{7}$$

In the case of power-law viscoplasticity, the effective potentials $\tilde{w}$ and $\tilde{w}_h$ also inherit the homogeneity of degree $1+1/n$ and $-1/n$ in $\bar{\boldsymbol{D}}$ and $\dot{\gamma}_0$ from the local potential w. Therefore, we express the hydrostatic effective potential $\tilde{w}_h$ as

$$\tilde{w}_h(\bar{D}_m) = \frac{\dot{\gamma}_0\tilde{\sigma}_h}{1+1/n}\left|\frac{3\bar{D}_m}{\dot{\gamma}_0}\right|^{1+1/n}, \tag{8}$$

where $\tilde{\sigma}_h$ denotes an effective flow stress which depends on nonlinearity n, porosity f, flow stresses $\tau_0^{(k)}$ and Schmid tensors $\boldsymbol{\mu}^{(k)}$, but not on $\bar{D}_m$ and $\dot{\gamma}_0$, and completely characterizes the response of the voided crystal under hydrostatic loading. In the following sections we adopt different models to generate estimates for this effective property and to study the influence of the various material parameters on the effective response.

3. Hollow-sphere assemblages

3.1. Power-law viscoplasticity

Following an approach initiated by Gurson (1977), the representative volume element is taken here to be an assemblage of an infinite number of homothetic hollow spheres filling up the entire volume (see, for instance, Gărăjeu et al., 2000). For this microgeometry, a velocity field corresponding to a homogeneous radial expansion of all spheres is kinematically compatible. An upper bound for the effective dissipation potential can thus be obtained by evaluating the local potential within any given sphere at a velocity field of the form

$$\boldsymbol{u}(\boldsymbol{x}) = \bar{D}_m\frac{b^3}{r^2}\boldsymbol{\xi}, \tag{9}$$

where b is the radius of the sphere, $r = |\boldsymbol{x}|$, $\boldsymbol{\xi} = \boldsymbol{x}/|\boldsymbol{x}|$, and $\boldsymbol{x}$ is the position vector relative to the center of the sphere. The local strain-rate is then given by

$$\boldsymbol{D}(\boldsymbol{x}) = -3\bar{D}_m\frac{b^3}{r^3}\,\boldsymbol{\xi}\otimes_d\boldsymbol{\xi}. \tag{10}$$

Thus, the effective dissipation potential is bounded from above by

$$\tilde{w}_h(\bar{D}_m) \le (1-f)\frac{1}{(4/3)\pi(b^3-a^3)}\int_S\int_a^b w\left(3\bar{D}_m\frac{b^3}{r^3}\boldsymbol{\xi}\otimes_d\boldsymbol{\xi}\right) r^2\,\mathrm{d}r\mathrm{d}S(\boldsymbol{\xi}), \tag{11}$$

where S is the unit sphere and a is the void radius so that $f = (a/b)^3$. In view of the homogeneity of w in $\boldsymbol{D}$, the radial integration, and the power-law form (8) of the effective potential, we have that

$$\tilde{\sigma}_h \le \alpha_{HSA}(n)n\left(f^{-1/n}-1\right), \tag{12}$$

where

$$\alpha_{HSA}(n) = \frac{n+1}{n}\dot{\gamma}_0^{1/n}\left\langle w\left(\boldsymbol{\xi}\otimes_d\boldsymbol{\xi}\right)\right\rangle. \tag{13}$$

In this last expression, $\langle\cdot\rangle = (4\pi)^{-1}\int_S\cdot\,\mathrm{d}S(\boldsymbol{\xi})$ represents an orientational average over the unit sphere. Alternatively, this function can be written in terms of the dual potential as

$$\alpha_{HSA}(n) = \frac{n+1}{n}\left\langle\sup_{\boldsymbol{\sigma}_d\in\mathcal{T}_d}\left[\boldsymbol{\sigma}_d\cdot(\boldsymbol{\xi}\otimes_d\boldsymbol{\xi}) - \sum_{k=1}^{K}\frac{\tau_0^{(k)}}{n+1}\left|\frac{\boldsymbol{\sigma}_d\cdot\boldsymbol{\mu}^{(k)}}{\tau_0^{(k)}}\right|^{n+1}\right]\right\rangle. \tag{14}$$

In turn, this expression can be simplified by exploiting the homogeneity of degree $n+1$ in $\boldsymbol{\sigma}_d$ of the dual potential. Indeed, evaluating the objective function at $\lambda\boldsymbol{\sigma}_d$ and optimizing with respect to λ we obtain

$$\alpha_{HSA}(n) = \left\langle\sup_{\boldsymbol{\sigma}_d\in\mathcal{T}_d}\frac{|\boldsymbol{\xi}\cdot\boldsymbol{\sigma}_d\boldsymbol{\xi}|^{\frac{n+1}{n}}}{\left[\sum_{k=1}^{K}\tau_0^{(k)-n}\left|\boldsymbol{\sigma}_d\cdot\boldsymbol{\mu}^{(k)}\right|^{n+1}\right]^{\frac{1}{n}}}\right\rangle. \tag{15}$$

Note that the objective function in this last expression is homogeneous of degree zero in $\boldsymbol{\sigma}_d$, and consequently the admisible set can be restricted to tensors of fixed norm. Expressions (12)–(15) provide a Gurson-type estimate for the hydrostatic flow stress of a voided cubic crystal. The estimate exhibits the same functional dependence on porosity as Gurson's estimate for a von Mises voided solid (cf. Michel and Suquet, 1992), and depends on the plastic anisotropy of the crystal only through the prefactor $\alpha_{HSA}(n)$.

3.2. Linear viscosity

When the creep exponent is $n = 1$, the bound (12) for the hydrostatic flow stress yields the following bound for the viscous compressibility $\tilde{\kappa} = \dot{\gamma}_0^{-1}\tilde{\sigma}_h$:

$$\tilde{\kappa} \le \dot{\gamma}_0^{-1}\alpha_{HSA}(1)\frac{1-f}{f}, \tag{16}$$

where the prefactor $\alpha_{HSA}(1)$ is given by

$$\dot{\gamma}_0^{-1}\alpha_{HSA}(1) = \frac{2}{15}\mathbb{K}\cdot\mathbb{L}, \tag{17}$$

and $\mathbb{K}$ is the standard fourth-order incompressible projection tensor.

3.3. Ideal plasticity

In the limit $n\to\infty$, the upper bound (12) becomes

$$\tilde{\sigma}_h \le -\beta_{HSA}\ln f, \tag{18}$$

where

$$\beta_{HSA} = \lim_{n\to\infty}\alpha_{HSA}(n) = \left\langle\sup_{\boldsymbol{\sigma}_d\in\mathcal{P}}\boldsymbol{\xi}\cdot\boldsymbol{\sigma}_d\boldsymbol{\xi}\right\rangle \tag{19}$$

Expressions (18) and (19) provide a Gurson-type estimate for the hydrostatic strength of a voided cubic crystal. This estimate recovers that of Paux et al. (2015) for face-centered cubic crystals with all slip strengths equal, and that of Gurson (1977) for von Mises voided solids.

3.4. Deficient crystals

When the set of Schmid tensors $\boldsymbol{\mu}^{(k)}$ has *less than five* linearly independent systems and does not span the entire set of deviatoric tensors $\mathcal{T}_d$ the crystal cannot accommodate an arbitrary deformation and is said to be deficient. In this case, the estimate (14) can be shown to be infinitely large. This is because if a crystal is deficient there are tensors in $\mathcal{T}_d$ that are orthogonal to all Schmid tensors, and therefore the supremum in (14) becomes unbounded. Indeed, let $\boldsymbol{\mu}_0$ be one such tensor, so that $\boldsymbol{\mu}_0 \cdot \boldsymbol{\mu}^{(k)} = 0$ for $k = 1, \dots, K$. Restricting the admissible set in (14) to the subset of tensors of the form

$$\boldsymbol{\sigma}_d = \lambda \boldsymbol{\xi} \cdot \boldsymbol{\mu}_0 \boldsymbol{\xi}\ \boldsymbol{\mu}_0 \tag{20}$$

we obtain the lower bound

$$\alpha_{HSA}(n) \geq \frac{n+1}{n} \sup_{\lambda \in \mathbb{R}} \lambda \left\langle \left(\boldsymbol{\xi} \cdot \boldsymbol{\mu}_0 \boldsymbol{\xi} \right)^2 \right\rangle. \tag{21}$$

Given that the orientational average in this expression is strictly positive, the supremum over λ is unbounded and therefore

$$\alpha_{HSA}(n) = +\infty. \tag{22}$$

Thus, the estimate (14) based on hollow-sphere assemblages predicts that any deficient voided crystal is rigid under hydrostatic loading.

4. Infinite-rank sequential laminates

4.1. Power-law viscoplasticity

Following Idiart (2008), the representative volume element is taken here to be a sequential laminate of infinite rank. A sequential laminate is an iterative construction obtained by layering laminated materials (which in turn have been obtained from lower-order lamination procedures) with other laminated materials, or directly with the homogeneous phases that make up the multiphase solid, in such a way as to produce hierarchical microstructures of increasing complexity. The rank of the laminate refers to the number of layering operations required to reach the final sequential laminate. Two-phase sequential laminates of the matrix-inclusion type can be formed by layering at every step a two-phase laminate with the matrix phase. In this work we adopt the isotropic lamination sequence proposed by Idiart (2008). The resulting dissipation potential is given by

$$\tilde{w}(\bar{\boldsymbol{D}}) = \hat{w}(\bar{\boldsymbol{D}}, -\ln f) \tag{23}$$

where the function $\hat{w}(\boldsymbol{D}, \tau)$ is solution to the initial-value Hamilton-Jacobi equation

$$\begin{aligned} &\partial_\tau \hat{w} + \hat{w} + \left\langle \sup_{\boldsymbol{a}} \left[\partial_{\boldsymbol{D}} \hat{w} \cdot (\boldsymbol{a} \otimes_s \boldsymbol{\xi}) - w(\boldsymbol{D} + \boldsymbol{a} \otimes_s \boldsymbol{\xi}) \right] \right\rangle = 0, \\ &\hat{w}(\boldsymbol{D}, 0) = 0. \end{aligned} \tag{24}$$

In view of the incompressibility of the matrix phase, the argument of w in this equation must be traceless. Thus, the optimal $\boldsymbol{a}$ must be of the form

$$\boldsymbol{a} = -\mathrm{tr}\boldsymbol{D}\ \boldsymbol{\xi} + \boldsymbol{a}_\perp, \tag{25}$$

where $\boldsymbol{a}_\perp$ is orthogonal to $\boldsymbol{\xi}$. Thus,

$$\begin{aligned} \partial_\tau \hat{w}\ \ &+ \hat{w} + \left\langle \sup_{\boldsymbol{a}_\perp \in \mathcal{A}_\perp(\boldsymbol{\xi})} \left[\partial_{\boldsymbol{D}} \hat{w} \cdot (-\mathrm{tr}\boldsymbol{D}\ \boldsymbol{\xi} \otimes \boldsymbol{\xi} + \boldsymbol{a}_\perp \otimes_s \boldsymbol{\xi}) \right.\right. \\ &\left.\left. - w(-\mathrm{tr}\boldsymbol{D}\ \boldsymbol{\xi} \otimes_d \boldsymbol{\xi} + \boldsymbol{D}_d + \boldsymbol{a}_\perp \otimes_s \boldsymbol{\xi}) \right] \right\rangle = 0, \end{aligned} \tag{26}$$

where $\mathcal{A}_\perp(\boldsymbol{\xi}) = \left\{ \boldsymbol{a}_\perp \in \mathbb{R}^3 \ :\ \boldsymbol{a}_\perp \cdot \boldsymbol{\xi} = 0 \right\}$. The function $\hat{w}$ inherits the cubic symmetry of the local potential w; therefore, it is such that

$$\partial_{\boldsymbol{D}} \hat{w}(D_m \boldsymbol{I}, \tau) = \frac{1}{3} \partial_{D_m} \hat{w}(D_m \boldsymbol{I}, \tau) \boldsymbol{I} \equiv \frac{1}{3} \partial_{D_m} \hat{w}_h(D_m, \tau) \boldsymbol{I}, \tag{27}$$

where $\hat{w}_h(D_m, \tau) \doteq \hat{w}(D_m \boldsymbol{I}, \tau)$. In view of this property, Eq. (26) can be integrated along spherical strain rates (i.e., $\boldsymbol{D}_d = \boldsymbol{0}$). Thus, the function $\hat{w}_h$ is solution to the reduced Hamilton-Jacobi equation

$$\begin{aligned} &\partial_\tau \hat{w}_h + \hat{w}_h - D_m \partial_{D_m} \hat{w}_h - \left\langle \inf_{\boldsymbol{a}_\perp \in \mathcal{A}_\perp(\boldsymbol{\xi})} w(-3D_m \boldsymbol{\xi} \otimes_d \boldsymbol{\xi} + \boldsymbol{a}_\perp \otimes_s \boldsymbol{\xi}) \right\rangle \\ &\qquad = 0, \quad \hat{w}_h(D_m, 0) = 0. \end{aligned} \tag{28}$$

The function $\hat{w}_h$ also inherits the homogeneity of degree $1 + 1/n$ and $-1/n$ in $\boldsymbol{D}$ and $\dot{\gamma}_0$ of the local potential w. Thus, it can be written as

$$\hat{w}_h(D_m, \tau) = \frac{\hat{\sigma}_h(\tau)\dot{\gamma}_0}{1 + 1/n} \left| \frac{3D_m}{\dot{\gamma}_0} \right|^{1+1/n}. \tag{29}$$

Upon inserting this expression into (28) we obtain an ordinary differential equation for the function $\hat{\sigma}_h(\tau)$:

$$\partial_\tau \hat{\sigma}_h - \frac{1}{n} \hat{\sigma}_h - \alpha_{LAM}(n) = 0, \quad \hat{\sigma}_h(0) = 0, \tag{30}$$

where the function $\alpha_{LAM}(n)$ is given by

$$\alpha_{LAM}(n) = \frac{1+n}{n} \dot{\gamma}_0^{1/n} \left\langle \inf_{\boldsymbol{a}_\perp \in \mathcal{A}_\perp(\boldsymbol{\xi})} w(\boldsymbol{\xi} \otimes_d \boldsymbol{\xi} + \boldsymbol{a}_\perp \otimes_s \boldsymbol{\xi}) \right\rangle. \tag{31}$$

Integration of (30) yields

$$\hat{\sigma}_h(\tau) = \alpha_{LAM}(n) n \left(e^{\tau/n} - 1 \right), \tag{32}$$

and recalling that $\tilde{\sigma}_h = \hat{\sigma}_h(-\ln f)$ we finally obtain

$$\tilde{\sigma}_h = \alpha_{LAM}(n) n \left(f^{-1/n} - 1 \right). \tag{33}$$

This expression provides an estimate for the hydrostatic flow stress of a voided cubic crystal. The functional dependence on porosity is exactly the same as that obtained in the previous section for hollow-sphere assemblages, but the prefactor $\alpha_{LAM}(n)$ is different from $\alpha_{HSA}(n)$. In fact, it is evident from expressions (13) and (31) that $\alpha_{LAM}(n) \leq \alpha_{HSA}(n)$.

For computational purposes it is convenient to write the function α_{LAM} in terms of the dual stress potential as

$$\begin{aligned} \alpha_{LAM}(n) = \frac{1+n}{n} \Bigg\langle \inf_{\boldsymbol{a}_\perp \in \mathcal{A}_\perp(\boldsymbol{\xi})} \sup_{\boldsymbol{\sigma}_d \in \mathcal{T}_d} \Big[&\boldsymbol{\sigma}_d \cdot (\boldsymbol{\xi} \otimes_d \boldsymbol{\xi} + \boldsymbol{a}_\perp \otimes_s \boldsymbol{\xi}) \\ &- \sum_{k=1}^{K} \frac{\tau_0^{(k)}}{n+1} \left| \frac{\boldsymbol{\sigma}_d \cdot \boldsymbol{\mu}^{(k)}}{\tau_0^{(k)}} \right|^{n+1} \Big] \Bigg\rangle. \end{aligned} \tag{34}$$

The infimum condition with respect to $\boldsymbol{a}_\perp$ in this expression requires that $\boldsymbol{\sigma}_d \boldsymbol{\xi} \,||\, \boldsymbol{\xi}$; thus,

$$\begin{aligned} &\alpha_{LAM}(n) \\ &= \frac{1+n}{n} \left\langle \sup_{\boldsymbol{\sigma}_d \in \mathcal{T}_{||}(\boldsymbol{\xi})} \left[\boldsymbol{\sigma}_d \cdot (\boldsymbol{\xi} \otimes_d \boldsymbol{\xi}) - \sum_{k=1}^{K} \frac{\tau_0^{(k)}}{n+1} \left| \frac{\boldsymbol{\sigma}_d \cdot \boldsymbol{\mu}^{(k)}}{\tau_0^{(k)}} \right|^{n+1} \right] \right\rangle, \end{aligned} \tag{35}$$

where $\mathcal{T}_{||}(\boldsymbol{\xi}) = \left\{ \boldsymbol{\sigma}_d \in \mathcal{T}_d \ :\ \boldsymbol{\sigma}_d \boldsymbol{\xi} \,||\, \boldsymbol{\xi} \right\}$. Once again, this expression can be simplified by evaluating the objective function at $\lambda \boldsymbol{\sigma}_d$ and optimizing with respect to λ; we obtain

$$\alpha_{LAM}(n) = \left\langle \sup_{\boldsymbol{\sigma}_d \in \mathcal{T}_{||}(\boldsymbol{\xi})} \frac{|\boldsymbol{\xi} \cdot \boldsymbol{\sigma}_d \boldsymbol{\xi}|^{\frac{n+1}{n}}}{\left[\sum_{k=1}^{K} \tau_0^{(k)-n} \left| \boldsymbol{\sigma}_d \cdot \boldsymbol{\mu}^{(k)} \right|^{n+1} \right]^{\frac{1}{n}}} \right\rangle. \tag{36}$$

Note that the objective function in this last expression is homogeneous of degree zero in $\boldsymbol{\sigma}_d$, and consequently the admissible set can be restricted to tensors of fixed norm.

4.2. Linear viscosity

When the creep exponent is $n = 1$, the estimate (33) for the hydrostatic flow stress yields the following estimate for the viscous compressibility:

$$\tilde{\kappa} = \dot{\gamma}_0^{-1}\alpha_{LAM}(1)\frac{1-f}{f}, \tag{37}$$

where the prefactor $\alpha_{LAM}(1)$ is given by

$$\dot{\gamma}_0^{-1}\alpha_{LAM}(1) = \frac{2}{15}\mathbb{K}\cdot\mathbb{L} - \left\langle \frac{A_{22}A_1^2 + A_{11}A_2^2 - 2A_{12}A_1A_2}{A_{11}A_{22} - A_{12}^2}\right\rangle. \tag{38}$$

In this last expression, $A_{ij} = (\boldsymbol{\xi}\otimes\boldsymbol{\xi}_i)\cdot\mathbb{L}(\boldsymbol{\xi}\otimes\boldsymbol{\xi}_j)$, $A_i = (\boldsymbol{\xi}\otimes_d\boldsymbol{\xi})\cdot\mathbb{L}(\boldsymbol{\xi}\otimes\boldsymbol{\xi}_i)$, and $\{\boldsymbol{\xi}_1, \boldsymbol{\xi}_2, \boldsymbol{\xi}\}$ is an orthonormal basis for $\mathbb{R}^3$. The second term in this expression arises due to the constraint $\boldsymbol{\sigma}_d\boldsymbol{\xi}||\boldsymbol{\xi}$ in the definition of the set $\mathcal{T}_{||}(\boldsymbol{\xi})$. If the viscosity tensor $\mathbb{L}$ is isotropic, this term vanishes and the predictions based on sequential laminates and hollow sphere assemblages agree exactly. If the viscosity tensor $\mathbb{L}$ is anisotropic, by contrast, the second term is negative and $\alpha_{LAM}(1) < \alpha_{HSA}(1)$.

4.3. Ideal plasticity

In the limit $n\to\infty$, the estimate (33) becomes

$$\tilde{\sigma}_h = -\beta_{LAM}\ln f, \tag{39}$$

where

$$\beta_{LAM} = \lim_{n\to\infty}\alpha_{LAM}(n) = \left\langle \sup_{\boldsymbol{\sigma}_d\in\mathcal{P}_{||}(\boldsymbol{\xi})} \boldsymbol{\xi}\cdot\boldsymbol{\sigma}_d\boldsymbol{\xi}\right\rangle \tag{40}$$

in view of (35). In this last expression, $\mathcal{P}_{||}(\boldsymbol{\xi}) = \left\{\boldsymbol{\sigma}_d\in\mathcal{P} \;:\; \boldsymbol{\sigma}_d\boldsymbol{\xi} \;||\; \boldsymbol{\xi}\right\}$.

4.4. Deficient crystals

In the case of deficient crystals with *less than three* linearly independent slip systems, the estimate (34) can be shown to be infinitely large. Indeed, let $\boldsymbol{\mu}_1$, $\boldsymbol{\mu}_2$ and $\boldsymbol{\mu}_3$ be three linearly independent deviatoric tensors that are orthogonal to all Schmid tensors of the deficient crystal, so that $\boldsymbol{\mu}_i\cdot\boldsymbol{\mu}^{(k)} = 0$ for $k = 1,\dots,K$, and consider deviatoric tensors of the form

$$\begin{aligned}\boldsymbol{\sigma}_d = \lambda\;\boldsymbol{\xi}\cdot[f_1(\boldsymbol{\xi})\boldsymbol{\mu}_1 + f_2(\boldsymbol{\xi})\boldsymbol{\mu}_2 + f_3(\boldsymbol{\xi})\boldsymbol{\mu}_3]\boldsymbol{\xi}\\ \times\left[f_1(\boldsymbol{\xi})\boldsymbol{\mu}_1 + f_2(\boldsymbol{\xi})\boldsymbol{\mu}_2 + f_3(\boldsymbol{\xi})\boldsymbol{\mu}_3\right],\end{aligned} \tag{41}$$

where the functions f_i are given by

$$f_1(\boldsymbol{\xi}) = (\boldsymbol{\xi}_2\cdot\boldsymbol{\mu}_2\boldsymbol{\xi})(\boldsymbol{\xi}_1\cdot\boldsymbol{\mu}_3\boldsymbol{\xi}) - (\boldsymbol{\xi}_1\cdot\boldsymbol{\mu}_2\boldsymbol{\xi})(\boldsymbol{\xi}_2\cdot\boldsymbol{\mu}_3\boldsymbol{\xi}), \tag{42}$$

$$f_2(\boldsymbol{\xi}) = (\boldsymbol{\xi}_1\cdot\boldsymbol{\mu}_1\boldsymbol{\xi})(\boldsymbol{\xi}_2\cdot\boldsymbol{\mu}_3\boldsymbol{\xi}) - (\boldsymbol{\xi}_2\cdot\boldsymbol{\mu}_1\boldsymbol{\xi})(\boldsymbol{\xi}_1\cdot\boldsymbol{\mu}_3\boldsymbol{\xi}), \tag{43}$$

$$f_3(\boldsymbol{\xi}) = (\boldsymbol{\xi}_1\cdot\boldsymbol{\mu}_2\boldsymbol{\xi})(\boldsymbol{\xi}_2\cdot\boldsymbol{\mu}_1\boldsymbol{\xi}) - (\boldsymbol{\xi}_1\cdot\boldsymbol{\mu}_1\boldsymbol{\xi})(\boldsymbol{\xi}_2\cdot\boldsymbol{\mu}_2\boldsymbol{\xi}), \tag{44}$$

and the vectors $\boldsymbol{\xi}_i$ are such that $\{\boldsymbol{\xi}_1, \boldsymbol{\xi}_2, \boldsymbol{\xi}\}$ constitutes an orthonormal basis for $\mathbb{R}^3$ for a given $\boldsymbol{\xi}$. The tensors (41) are such that $\boldsymbol{\xi}_1\cdot\boldsymbol{\sigma}_d\boldsymbol{\xi} = \boldsymbol{\xi}_2\cdot\boldsymbol{\sigma}_d\boldsymbol{\xi} = 0$ and therefore belong to $\mathcal{T}_{||}(\boldsymbol{\xi})$. Thus, restricting the admissible set in (34) to the subset of tensors of that form we obtain the lower bound

$$\alpha_{LAM}(n) \geq \frac{n+1}{n}\sup_{\lambda\in\mathbb{R}}\lambda\left\langle\left(\boldsymbol{\xi}\cdot[f_1(\boldsymbol{\xi})\boldsymbol{\mu}_1 + f_2(\boldsymbol{\xi})\boldsymbol{\mu}_2 + f_3(\boldsymbol{\xi})\boldsymbol{\mu}_3]\boldsymbol{\xi}\right)^2\right\rangle. \tag{45}$$

Given that the orientational average in this expression is strictly positive, the supremum over λ is unbounded and therefore

$$\alpha_{LAM}(n) = +\infty. \tag{46}$$

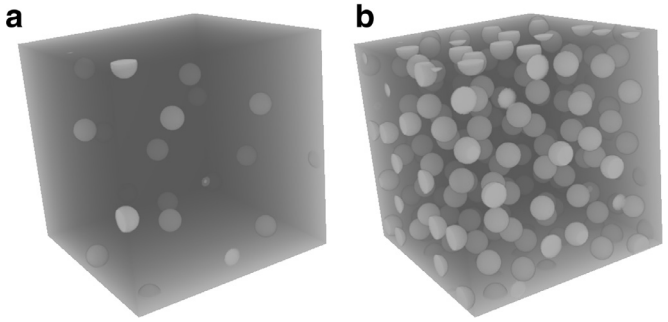

Fig. 1. Unit cells with isotropic dispersions of voids with radius $r = 0.05L$ and two porosity levels: (a) $f = 0.01$, (b) $f = 0.1$.

Thus, the estimate (34) based on sequential laminates predicts that any deficient voided crystal with less than three linearly independent systems is rigid under hydrostatic loading. It is emphasized, however, that this analysis does *not* carry over to deficient crystals with *three or more* linearly independent systems. In that case, there are less than three linearly independent deviatoric tensors that are orthogonal to all Schmid tensors of the deficient crystal, and consequently a subset of tensors analogous to (41) is not available.

5. Periodic media

5.1. The microstructure

The representative volume element is taken here to be a periodic medium with cubic unit cells. In order to assess the sensitivity of the effective properties to the particular void distribution, we consider unit cells with a single void at the center as well as with multiple voids isotropically distributed. Unit cells containing multiple voids are generated following a similar procedure to that of Vincent et al. (2014). First, a cubic cell of side length L is filled with N spheres following a random process constrained by a non-overlapping condition. All spheres have the same radius R and occupy a volume fraction of 0.35. Secondly, spherical voids of radius r are introduced at the center of each sphere. Each void and its surrounding shell of matrix constitute an elementary pattern. The total porosity is given by $f = (4/3)\pi(r/L)^3N$. Thus, the void radius r is selected so that the desired porosity level is produced with a reasonable number of patterns N. Representative unit cells are shown in Fig. 1.

5.2. An FFT algorithm

The mechanical fields within the unit cell are computed by means of a Fast-Fourier transform (FFT) algorithm originally proposed by Moulinec and Suquet (1994) and implemented in the computer code CraFT following Suquet et al. (2012). This algorithm solves a regularized version of the Euler-Lagrange equations associated with (6), as given by

$$\begin{aligned}&\mathrm{div}\boldsymbol{\sigma} = \mathbf{0}, \quad \dot{\boldsymbol{\sigma}} = \mathbb{C}\left(\boldsymbol{D} - \boldsymbol{D}^{vp}\right), \quad \boldsymbol{D}^{vp} = \frac{\partial u}{\partial\boldsymbol{\sigma}}(\boldsymbol{x},\boldsymbol{\sigma}),\\ &\boldsymbol{D} = \nabla\otimes_s\boldsymbol{u}, \quad \boldsymbol{u} = \overline{\boldsymbol{D}}\boldsymbol{x} + \boldsymbol{u}_{\#} \quad \text{in} \quad \Omega_{\#},\end{aligned} \tag{47}$$

along with periodic conditions on the boundary of the unit cell $\Omega_{\#}$ for the velocity field $\boldsymbol{u}_{\#}$. In these expressions, the stress potential u is given by $(2)_2$ in the matrix domain and is infinite within the voids, $\mathbb{C}$ is a fourth-order elasticity tensor that can be arbitrarily chosen, and the overdot denotes time differentiation. The specimens are assumed to be initially unstressed and are subject to a fixed macroscopic strain-rate. Under these conditions,

Eq. (47) are integrated in time without evolving the microstructure by means of a Runge–Kutta(3)2 FSAL method (e.g., Bogaki and Shampine, 1989) until the elastic strain rates become negligible and the mechanical fields approach those of the purely viscoplastic problem (6). At each step of the time integration, the mechanical fields are determined by a fixed point algorithm that iterates until the convergence criterion is met. This algorithm makes use of an FFT subroutine that discretizes the unit cell into a regular cubic array of voxels. Details on the procedure can be found, for instance, in Idiart et al. (2006).

To characterize the hydrostatic response of power-law viscoplastic crystals, the direction of macroscopic stress is prescribed as purely spherical following a procedure described in Michel et al. (1999), the spherical part of the macroscopic strain rate is set to a fixed value $\bar{D}_m > 0$, and the mechanical fields deep in the plastic range are determined. Then, the average hydrostatic stress $\bar{\sigma}_m$ over the unit cell is computed and the hydrostatic flow stress is finally obtained from the relation

$$\tilde{\sigma}_h = \bar{\sigma}_m \left| \frac{\dot{\gamma}_0}{3\bar{D}_m} \right|^{1/n}, \tag{48}$$

which follows from (7) and (8). The calculations reported in Section 6 have been carried out by setting $\bar{D}_m = 9000^{-1}\mathrm{s}^{-1}$ and $\dot{\gamma}_0 = 1\mathrm{s}^{-1}$, and identifying the elasticity tensor $\mathbb{C}$ with that of a stainless steel. It is emphasized, however, that the hydrostatic flow stress (48) is indifferent to the particular values employed for these parameters. Calculations were carried out using the so-called "basic scheme" which ensures strain compatibility, along with convergence criteria on the prescribed direction of the macroscopic stress and the local equilibrium condition.

6. Results and discussion

The above models are used in this section to generate predictions for the following three types of crystalline solids:

- Face-centered cubic (fcc) solids that deform plastically on a set of four slip planes of the type {111} along three slip directions (per plane) of type ⟨110⟩, which constitute a set of twelve slip systems ($K = 12$).
- Body-centered cubic (bcc) solids that deform through slip along the ⟨111⟩ directions on the {110} and {112} planes, which constitute a set of twenty-four slip systems ($K = 24$).
- Ionic solids that deform plastically on three different families of slip systems: {110} ⟨110⟩, {100} ⟨110⟩, {111} ⟨110⟩. They will be referred to as *A*, *B* and *C* families, respectively. The *A* family consists of six systems, among which two are linearly independent and can accommodate only normal components of strain rate —relative to the cubic axes of the crystal. The *B* family consists of six systems, among which three are linearly independent and can only accommodate shear components of strain rate —relative to the cubic axes of the crystal. Because of the orthogonality of the *A* and *B* systems, the two families together provide five independent slip systems so that a general isochoric deformation can be accommodated. The *C* family, in turn, consists of the same twelve slip systems of an FCC crystal. Thus, the three families together consist of twenty-four slip systems ($K = 24$).

6.1. Weakly anisotropic crystals

In this subsection we consider fcc, bcc and ionic crystals with $\tau_0^{(k)} = \tau_0$ for all k. These are all crystals exhibiting a relatively weak plastic anisotropy. Moreover, in view of the isotropic symmetry of void dispersion and macroscopic loading, the overall plastic dissipation is equipartitioned among all slip systems.

Table 1
Prefactors α_{HSA} and α_{LAM}, normalized by τ_0, for weakly anisotropic crystals with various creep exponents n.

	fcc		bcc		ionic	
	α_{HSA}	α_{LAM}	α_{HSA}	α_{LAM}	α_{HSA}	α_{LAM}
$n = 1$	0.733	0.651	0.367	0.321	0.316	0.298
$n = 2$	1.266	1.165	0.898	0.815	0.767	0.746
$n = 3$	1.500	1.397	1.191	1.093	1.011	0.990
$n = 5$	1.700	1.597	1.468	1.357	1.239	1.215
$n = 10$	1.859	1.743	1.685	1.557	1.418	1.386
$n \to \infty$	2.038	1.864	1.859	1.736	1.604	1.525

Table 2
FFT predictions for the hydrostatic flow stress $\tilde{\sigma}_h$, normalized by τ_0, of periodic fcc crystals with $\tau_0^{(k)} = \tau_0$, $f = 0.01$ and $n = 10$, and various microgeometries. Values for the random microgeometries correspond to 256^3 voxels, while the value for the single void at the center was obtained by interpolation, so that all values correspond to discretizations of 13 voxels per void radius.

seed 1	seed 2	seed 3	single void
9.701	9.674	9.667	9.649

We begin by comparing the prefactors $\alpha_{HSA}(n)$ and $\alpha_{LAM}(n)$ associated with hollow-sphere assemblages and sequential laminates, for the various plastic anisotropies. Table 1 reports numerical values of these prefactors for typical values of the creep exponent n, while Fig. 2(a) shows plots for the prefactors for the entire range of n. Details on the various numerical techniques employed in their computation are given in Appendix A. As anticipated in Section 4, sequential laminates are always softer than hollow-sphere assemblages. The differences, however, are not substantial: they are in the order of 10% for most cases and do not exceed 15%. In the case of ideally plastic crystals, both estimates predict prefactors in the range between 3/2 and 2 for the three crystal symmetries.

Next, we consider full-field simulations for periodic media. A sensitivity study is first carried out to determine the influence of the void dispersion and the FFT discretization size on the results. The main parameter governing convergence of the FFT results is actually the number of voxels lying within the voids. To select this number, FFT simulations with various discretization sizes (16^3, 32^3, 64^3, 128^3, 256^3) were carried out for an fcc crystal with porosity $f = 0.01$, creep exponent $n = 10$, and a unit cell containing a single void at the center. Fig. 2(b) shows the hydrostatic flow stress versus number of voxels. The results suggest that discretizations delivering at least 13 voxels per void radius provide a reasonable compromise between accuracy and computational demand. Consequently, the random unit cells employed in the sequel were discretized into 256^3 voxels and the radius of the voids was set to $r = 0.05L$ so that the number of voxels per void radius satisfies the above criterion. The hydrostatic flow stress of three such unit cells generated from different random seeds are reported in Table 2. The table also reports the value that would be obtained with a unit cell containing a single void at the center with a radius of 13 voxels, which was obtained by interpolating the values reported in Fig. 2(b). The four values are seen to be very similar: relative differences amount to less than 1%. Similar results have been found for other values of porosity up to ten percent. Thus, the hydrostatic flow stress seems to be relatively insensitive to the details of void dispersion, at least for monodisperse distributions with low to moderate porosity levels. In view of these results, the FFT results reported below correspond to one particular dispersion rather than to an average over various dispersions.

The estimates and the full-field simulations are confronted in Fig. 3. Plots for the effective flow stress are given versus creep exponent and porosity, for the three types of plastic anisotropies. Overall, the estimates are seen to be in good agreement with the

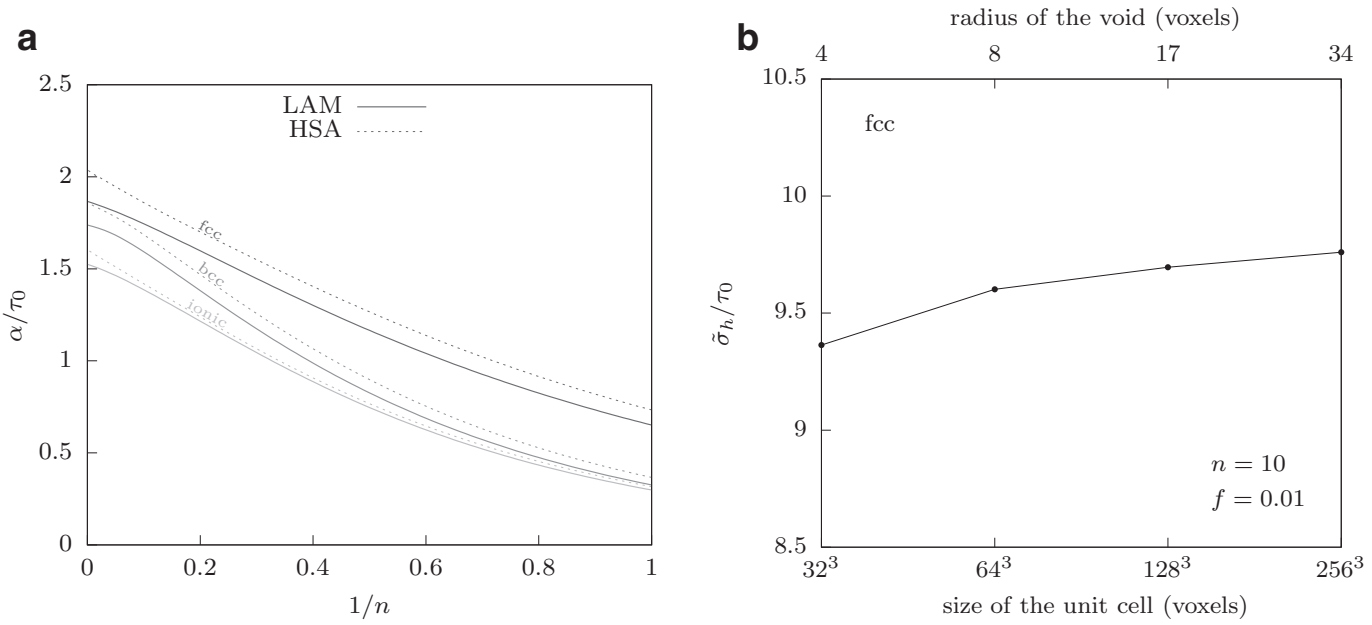

Fig. 2. Results for weakly anisotropic crystals with $\tau_0^{(k)} = \tau_0$ for all slip systems: (a) prefactors α_{LAM} and α_{HSA} as a function of creep exponent (n) for fcc, bcc and ionic crystals; (b) Hydrostatic flow stress $\tilde{\sigma}_h$ of an fcc unit cell with a single void at the center, porosity $f = 0.01$ and creep exponent $n = 10$, as a function of FFT discretization size.

simulations for the entire range of material parameters considered, including large values of the creep exponent. Thus, the simulations confirm the trend $\tilde{\sigma}_h \sim n(f^{-1/n} - 1)$ predicted by the estimates. It is recalled that this is the same trend exhibited by Gurson-type estimates for von Mises voided solids. The simulations also agree with the estimates in that the fcc crystals are stronger than the bcc and ionic crystals, as expected from the fact that the former crystals have the smaller number of slip systems. Also included in Fig. 3(a) are the finite-element results of Han et al. (2013) and of Mbiakop et al. (2015) for single- and monodisperse-voided fcc crystals, respectively. These results are seen to be entirely consistent with the present results for low porosity levels up to $f = 0.05$, thus confirming the low sensitivity of the hydrostatic flow stress to details of the void dispersion.

We conclude this discussion by recalling that the sequential laminates considered in this work attain the linear upper bound of Hashin and Shtrikman (see Idiart, 2008), which constitutes a rigorous upper bound on the hydrostatic flow stress of all crystals with an isotropic void dispersion and creep exponent $n = 1$. Estimates based on hollow sphere assemblages are thus seen to violate this bound.

6.2. Strongly anisotropic crystals

We now consider voided crystals with strong plastic anisotropy. In particular, we consider ionic crystals deforming by slip along the A and B families only. The flow stress of each family is denoted by τ_0^A and τ_0^B. Given the increased computational demand of the FFT simulations for these material systems, the discretization size was reduced to 128^3 and the void radius was set to a larger value ($r = 0.08L$) in order to preserve the number of voxels per void radius in the order of ten. For the larger plastic anisotropies, the convergence criteria were retained but the time steps had to be refined.

Fig. 4 shows plots for the hydrostatic flow stress versus slip contrast, for the choice $f = 0.01$ and various creep exponents. We begin by noting that the FFT results show a monotonic increase of the hydrostatic flow stress with increasing slip contrast, as expected, albeit with different asymptotic behavior depending on the family of slip systems exhibiting the stronger flow stress. When $\tau_0^B > \tau_0^A$ the FFT results seem to grow linearly with the ratio τ_0^B/τ_0^A for all values of n, but when $\tau_0^A > \tau_0^B$ they seem to grow sublinearly with the ratio τ_0^A/τ_0^B for all values of n and even asymptote to a finite value as $\tau_0^A/\tau_0^B \to \infty$. It should be recalled that as these ratios tend to infinity the crystal becomes plastically deficient: the limit $\tau_0^B \to \infty$ corresponds to a crystal deforming along slip systems belonging to the A family only, which has two linearly independent systems, while the limit $\tau_0^A \to \infty$ corresponds to a crystal deforming along slip systems belonging to the B family only, which has three linearly independent systems. Thus, the FFT results suggest that voided crystals with two linearly independent systems may be rigid under hydrostatic loading, while those with three linearly independent systems may dilate. Interestingly, this is in line with a recent study on voided *polycrystals* based on linear-comparison homogenization techniques (Nervi and Idiart, 2015). On the other hand, theoretical predictions and finite element simulations for hexagonal voided crystals with complex unit cells provided in Mbiakop et al. (2015) suggest that crystals with three linearly independent systems may be rigid under hydrostatic loading. However, spherical loadings in the context of hexagonal voided crystals do not possess the same significance as in the context of cubic voided crystals, since the ensuing deformation is not spherical. Unfortunately, all these full-field simulations are numerically demanding, making it difficult to conclusively infer the predicted response of deficient voided crystals by extrapolation.

In any case, the comparisons provided in Fig. 4 clearly show that estimates based on sequential laminates can be significantly more accurate than estimates based on hollow-sphere assemblages once the plastic anisotropy is strong. This is a consequence of the different asymptotic behaviors exhibited by these two estimates as the slip contrast tends to infinity. On the one hand, estimates based on hollow-sphere assemblages are seen to grow linearly as either slip ratio τ_0^A/τ_0^B and τ_0^B/τ_0^A tend to infinity; it was already shown in Section 3.4 that these estimates indeed become unbounded whenever the crystal is deficient. On the other hand, estimates based on sequential laminates grow linearly with the ratio τ_0^B/τ_0^A but sublinearly with the inverse ratio τ_0^A/τ_0^B. Moreover, in the latter case, their growth rate seems to decrease with in-

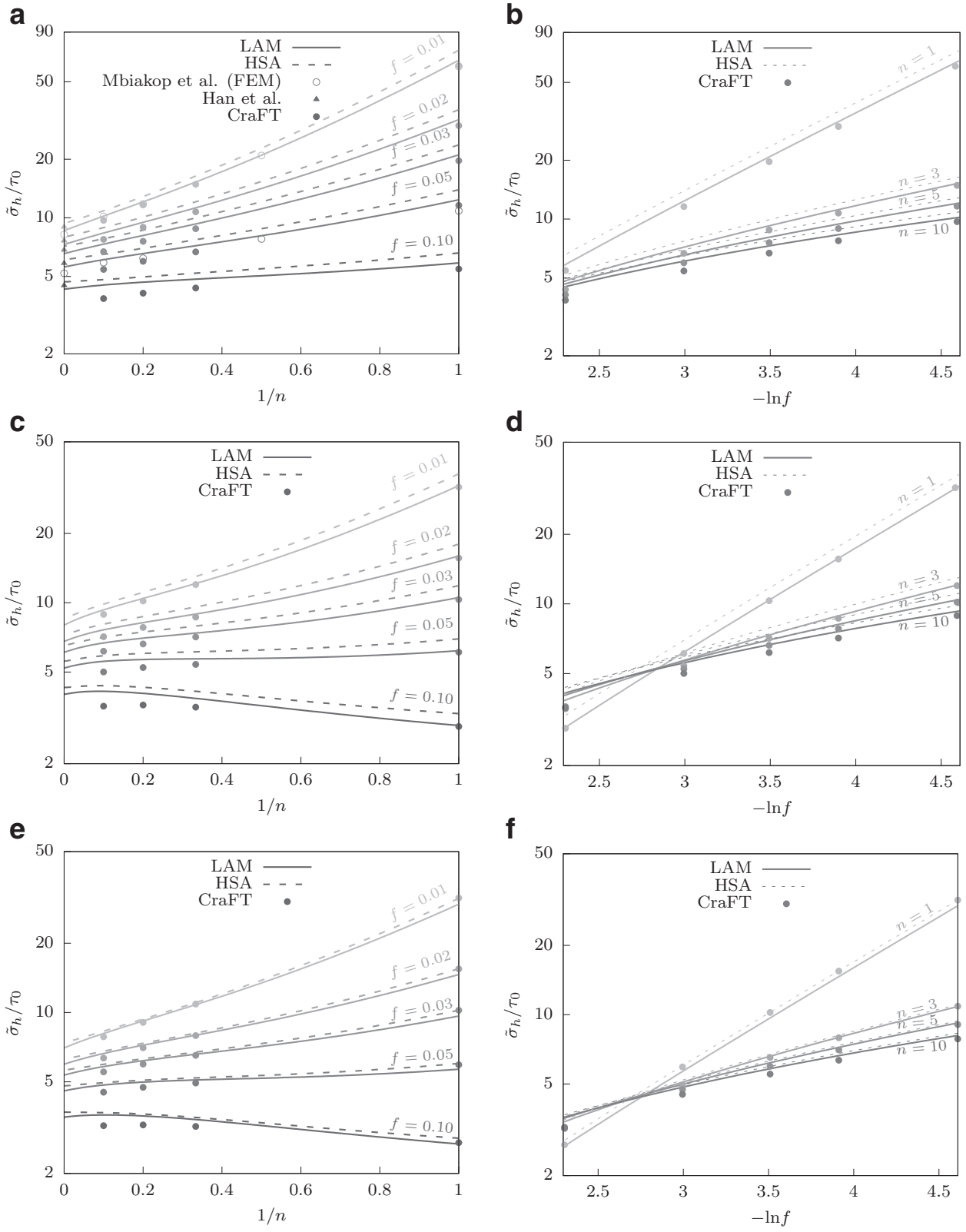

Fig. 3. Predictions for the hydrostatic flow stress $\tilde{\sigma}_h$ of weakly anisotropic voided crystals, normalized by τ_0, as a function of porosity f and creep exponent n: (a) & (b) fcc crystals, (c) & (d) bcc crystals, (e) and (f) ionic crystals.

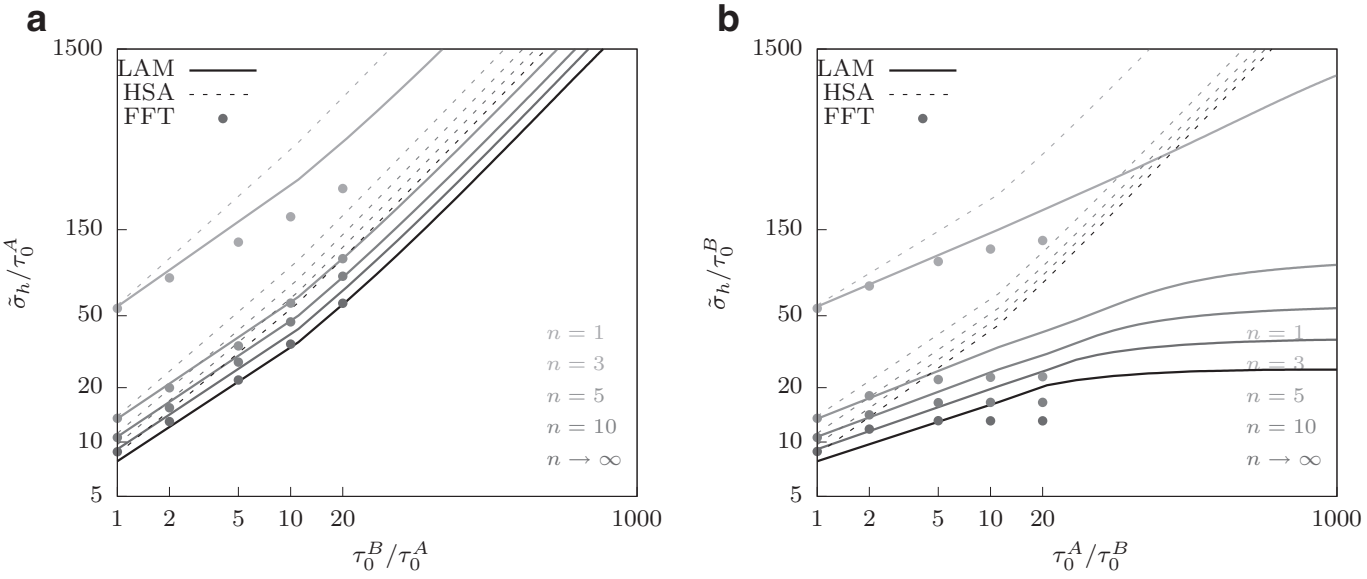

Fig. 4. Predictions for the hydrostatic flow stress $\tilde{\sigma}_h$ of ionic voided crystals deforming along the A and B families only, as a function of slip contrast, for $f = 0.01$ and various creep exponents n.

creasing creep exponent, and for the larger values of n they seem to asymptote to a finite value as τ_0^A/τ_0^B tends to infinity, in stark contrast with estimates based on hollow-sphere assemblages. It was already shown in Section 4.4 that these estimates become unbounded whenever a deficient crystal has less than three linearly independent systems. The estimates shown in Fig. 4(b) suggest that this may not be the case for deficient crystals with three or more linearly independent systems, in line with the FFT results. Unfortunately, this qualitative agreement with the FFT results is not accompanied by a quantitative agreement at the largest values of slip contrast where the response is likely to become very sensitive to the details of the microstructure. In this connection, it is recalled that the sequential laminates exhibit a uniform strain-rate field within the voided phase (Idiart, 2008) and can therefore deliver overly strong predictions for situations where the strain-rate field tends to localize along paths seeking out the voids (Idiart et al., 2006; 2009).

Regardless of the limiting behavior of the various predictions for deficient crystals, it is concluded that, overall, estimates based on sequential laminates are superior to Gurson-type based on hollow-sphere assemblages and predict the hydrostatic response of cubic voided crystals with reasonable accuracy, even for relatively strong plastic anisotropies. Whether these estimates remain accurate for more general loading conditions is currently under investigation.

Acknowledgments

This work was funded by IRSN through research contract DAFCJ/SJ/LS 20137 with LMA and UNLP. Additional funding was received by M.I.I. from UNLP through grant I-2017-225. We thank A. Mbiakop and K. Danas for providing the FEM results reported in Fig. 3(a).

Appendix A. Numerical computation of the prefactors α_{HSA} and α_{LAM}

To compute the prefactor α_{HSA} as given by (14) we carry out the integration over the unit sphere by letting $\boldsymbol{\xi}$ be the radius vector of a spherical coordinate system, adopting the polar and azimuth angles of that system as integration variables, and making use of Gaussian quadrature with 30 points per integration variable. To carry out the supremum over $\boldsymbol{\sigma}_d \in \mathcal{T}_d$ at each point $\boldsymbol{\xi}$ on the unit sphere, we express the elements of the set $\mathcal{T}_d$ as

$$\boldsymbol{\sigma}_d = \sum_{\alpha=1}^{5} \sigma_\alpha \boldsymbol{\eta}_\alpha, \tag{A.1}$$

where the $\boldsymbol{\eta}_\alpha$ constitute a Woo basis of the form

$$\boldsymbol{\eta}_1 = \frac{1}{\sqrt{6}}(2\boldsymbol{\xi}\otimes\boldsymbol{\xi} - \boldsymbol{\xi}_1\otimes\boldsymbol{\xi}_1 - \boldsymbol{\xi}_2\otimes\boldsymbol{\xi}_2),$$
$$\boldsymbol{\eta}_2 = \frac{1}{\sqrt{2}}(\boldsymbol{\xi}_1\otimes\boldsymbol{\xi}_1 - \boldsymbol{\xi}_2\otimes\boldsymbol{\xi}_2),$$
$$\boldsymbol{\eta}_3 = \sqrt{2}\boldsymbol{\xi}_1\otimes_s\boldsymbol{\xi}_2, \quad \boldsymbol{\eta}_4 = \sqrt{2}\boldsymbol{\xi}_1\otimes_s\boldsymbol{\xi}, \quad \boldsymbol{\eta}_5 = \sqrt{2}\boldsymbol{\xi}_2\otimes_s\boldsymbol{\xi}.$$

Here, $\{\boldsymbol{\xi}_1, \boldsymbol{\xi}_2, \boldsymbol{\xi}\}$ is the natural basis of the spherical coordinate system employed. The objective function is then maximized with respect to the components σ_α by means of the Powell method built in the library OPTIMIZE (SciPy project) for PYTHON. In the limit $n \to \infty$, the constrained minimization in the prefactor β_{HSA}, as given by (19), is performed by the method of Constrained Optimization By Linear Approximation (COBYLA) also implemented in the library OPTIMIZE.

The prefactors α_{LAM} and β_{LAM}, as given by (35) and (40), are evaluated in a similar fashion, except that in view of the definition of the set $\mathcal{T}_{||}(\boldsymbol{\xi})$, the elements $\boldsymbol{\sigma}_d$ are decomposed as (A.1) with $\sigma_4 = \sigma_5 = 0$. Thus, the function α_{LAM} is numerically simpler to compute than the function α_{HSA}.

References

Benzerga, A., Besson, J., 2001. Plastic potentials for anisotropic porous solids. Eur. J. Mech. A/Solids 20, 397–434.
Benzerga, A., Leblond, J.B., 2010. Ductile fracture by void growth to coalescence. Adv. Appl. Mech. 44, 169–305.
Bogaki, P., Shampine, L.F., 1989. A 3(2) pair of Runge-Kutta formulas. Appl. Math. Lett. 2, 321–325.
de Botton, G., 2005. Transversely isotropic sequentially laminated composites in finite elasticity. J. Mech. Phys. Solids 53, 1334–1361.
de Botton, G., Ponte Castañeda, P., 1995. Variational estimates for the creep of behaviour of polycrystals. Proc. R. Soc. Lond. A 448, 121–142.
Ponte Castañeda, P., Suquet, S., 1998. Nonlinear composites. Adv. Appl. Mech. 34, 171–302.
Crépin, J., Bretheau, T., Caldemaison, D., 1996. Cavity growth and rupture of β-treated zirconium: a crystallographic model. Acta Mater. 44, 4927–4935.

Danas, K., Idiart, M.I., Ponte Castañeda, P., 2008. A homogenization-based constitutive model for isotropic viscoplastic porous media. Int. J. Solids Struct. 45, 3392–3409.
Garner, F.A., 2012. Radiation damage in austenitic steels. Compr. Nuclear Mater. 4, 33–95.
Grennerat, F., Montagnat, M., Castelnau, O., Vacher, P., Moulinec, H., Suquet, P., Duval, P., 2012. Experimental characterization of the intragranular strain field in columnar ice during transient creep. Acta Mater. 60, 3655–3666.
Gurson, A.L., 1977. Continuum theory of ductile rupture by void nucleation and growth : part i - yield criteria. J. Eng. Mater. Technol. 99, 2–15.
Gărăjeu, M., Michel, J.C., Suquet, P., 2000. A micromechanical approach of damage in viscoplastic materials by evolution in size, shape and distribution of voids. Comput. Methods Appl. Mech. Eng. 183, 223–246.
Han, X., Besson, J., Forest, S., Tanguy, B., Bugat, S., 2013. A yield function for single crystals containing voids. Int. J. Solids Struct. 50, 2115–2131.
Idiart, M.I., 2007. Nonlinear sequential laminates reproducing hollow sphere assemblages. Comptes Rendus Mécanique 335, 363–368.
Idiart, M.I., 2008. Modeling the macroscopic behavior of two-phase nonlinear composites by infinite-rank laminates. J. Mech. Phys. Solids 56, 2599–2617.
Idiart, M.I., Moulinec, H., Ponte Castañeda, P., Suquet, P., 2006. Macroscopic behavior and field fluctuations in viscoplastic composites: second-order estimates vs full-field simulations. J. Mech. Phys. Solids 54, 1029–1063.
Idiart, M.I., Willot, F., Pellegrini, Y.P., Ponte Castañeda, P., 2009. Infinite-contrast periodic composites with strongly nonlinear behavior: effective-medium theory versus full-field simulations. Int. J. Solids Struct. 46, 3365–3382.
Mbiakop, A., Constantinescu, A., Danas, K., 2015. An analytical model for porous single crystals with ellipsoidal voids. J. Mech. Phys. Solids 84, 436–467.
Michel, J.-C., Suquet, P., 1992. The constitutive law of nonlinear viscous and porous materials. J. Mech. Phys. Solids 40, 74–98.
Michel, J.C., Moulinec, H., Suquet, P., 1999. Effective properties of composite materials with periodic microstructure: a computational approach. Comput. Methods Appl. Mech. Eng. 172, 109–143.
Moulinec, H., Suquet, P., 1994. A fast numerical method for computing the linear and nonlinear proprieties of composites. Compte-Rendu de l'Académie des Sciences Paris II 318, 1417–1423.
Ramos Nervi, J.E., Idiart, M.I., 2015. Bounding the plastic strength of polycrystalline voided solids by linear-comparison homogenization techniques. Proc. R. Soc. A 471, 20150380.
Paux, J., Morin, L., Brenner, R., Kondo, D., 2015. An approximate yield criterion for porous single crystals. Euro. J. Mech. A/Solids 51, 1–10.
Song, D., Ponte Castañeda, P., 2017. A finite-strain homogenization model for viscoplastic porous single crystals: I–theory. J. Mech. Phys. Solids 107, 560–579.
Srivastava, A., Needleman, A., 2013. Void growth versus void collapse in a creeping single crystal. J. Mech. Phys. Solids 61, 1169–1184.
Suquet, P., Moulinec, H., Castelnau, O., Montagnat, M., Lahellec, N., Grennerat, F., Duval, P., Brenner, R., 2012. Multi-scale modeling of the mechanical behavior of polycrystalline ice under transient creep. Proc. IUTAM 3, 76–90.
Vincent, P.-G., Suquet, P., Monerie, Y., Moulinec, H., 2014. Effective flow surface of porous materials with two populations of voids under internal pressure: II. full-field simulations. Int. J. Plast. 56, 74–98.
Yerra, S.K., Tekoglu, C., Scheyvaerts, L., Delannay, L., Van Houtte, P., Pardoen, T., 2010. Void growth and coalescence in single crystals. Int. J. Solids Struct. 47, 1016–1029.